Research Article

Multi-phase (Zr,Ti,Cr)B₂ solid solutions: Preparation, multi-scale microstructure, and local properties

Laura SILVESTRONI[a,*], Nicola GILLI[b], Alex SANGIORGI[a],
Alessandro COROZZI[a], Suzana FILIPOVIĆ[c], Nina OBRADOVIĆ[c],
Laia ORTIZ-MEMBRADO[d], Emilio JIMÉNEZ-PIQUÉ[d],
William G. FAHRENHOLTZ[e]

[a]*CNR-ISSMC, Institute of Science, Technology and Sustainability for Ceramics (former ISTEC),
Via Granarolo 64, 48018 Faenza, Italy*
[b]*CNR-IMM, Institute for Microelectronics and Microsystems, Via Gobetti 101, 40129 Bologna, Italy*
[c]*Institute of Technical Sciences of SASA, Knez Mihailova 35/IV, 11000 Belgrade, Serbia*
[d]*Department of Materials Science and Engineering, EEBE, Univ. Politècnica de
Catalunya-BarcelonaTECH. Avda. Eduard Maristany 16, 08019 Barcelona, Spain*
[e]*Department of Materials Science and Engineering, Missouri University of Science
and Technology, Rolla, MO 65049, USA*

Abstract: Multi-phase ceramics based on ZrB_2, TiB_2 and doped with CrB_2 and SiC were prepared by powder metallurgy and hot pressing to explore the possibility of obtaining multi-scale microstructures by super-saturation of complex $(Zr,Ti,Cr)B_2$ solid solutions. Core–shell structures formed in TiB_2 grains, whereas ZrB_2 appeared to form a homogeneous solid solution with the other metals. Precipitation of nano-inclusions within both micron-sized borides was assessed by transmission electron microscopy and thermodynamics elucidated the preferential formation of boride inclusions due to the specific sintering atmosphere. In addition, atomic size factors explicated the precipitation of CrB_2 nano-particles into ZrB_2-rich grains and of ZrB_2 nano-particles into TiB_2-rich grains. The hardness of the constituent phases measured by nanoindentation ranged from 36 to 43 GPa.

Keywords: boride; core–shell; solid solution; nanoindentation; sintering

1 Introduction

Hypersonic systems require materials that are able to survive heat fluxes of hundreds of Watts per square centimeter as well as aerodynamic and mechanical loads. Hypersonic technology allows aerospace vehicles to move more than 5 times the speed of sound, below traditional radar, and along unpredictable paths. Current missile defense systems would be ineffective against hypersonic vehicles. However, hypersonic defense systems that can successfully intercept, deflect, or destroy the incoming projectiles would offer a great technological step forward. Currently available materials suffer from technological limitations such as production

---

* Corresponding author.

E-mail: laura.silvestroni@istec.cnr.it

cost, weight ratios, or inability to perform under ablative heat fluxes. In view of their physical and structural properties, ultra-high temperature ceramics (UHTCs) are appealing candidates for defence applications, if suitable compositions can be identified and microstructure tailoring approaches can be developed. Among UHTCs, zirconium diboride ZrB_2 and titanium diboride TiB_2, combine strength and hot erosion resistance with favourable density and hardness [1–5]. Ceramics containing a combination of ZrB_2 and TiB_2 can be lower density alternatives to the more popular ZrB_2 and HfB_2 based ceramics. These ceramics may be able to protect components from heat and hot corrosion damage while also preserving their functionality.

With the aim of developing novel materials with reduced costs, improved mass efficiency, coupled with extended performance and lifetime of hypersonic systems, a multi-phase ceramic approach was undertaken. This work used ZrB_2 as major component, with TiB_2 added to reduce the density. Then, a third transition metal (TM) compound, CrB_2, was included to further reduce density and increase hardness [8,9]. In addition, SiC was added as additional hard phase based on its ability to promote the densification, forming a glassy protective phase upon oxidation, and minimal negative impact on high temperature strength for contents below 5 vol% [6,7,10].

The formation of a core–shell morphology has been identified as one of the key aspects to maintaining high strength at elevated temperatures [10–13]. The core–shell structure comprises a core with the nominally pure diboride grain seed, i.e., ZrB_2, and a solid solution shell that contains variable amounts of a second TM cation, i.e., $(Zr,TM)B_2$, as illustrated in Fig. 1. Using appropriate consolidation and post thermal treatment conditions, the shell morphology can be altered by the precipitation of nano-inclusions in the form of

TM-metal or -carbide [12]. These precipitates form within the boride grains and result in a hierarchical UHTC–TM hybrid structure consisting of homogeneously distributed nano-sized inclusions embedded in micron-sized grains. This hierarchical structure offers benefits in terms of increased local fracture toughness and strength, significant plastic deformation, and ability to maintain strength in the ultra-high temperature regime. Moreover, this structure has demonstrated improvements in the oxidation resistance behavior in the case of other borides, i.e., ZrB_2 and HfB_2 [14–17]. This approach has never been thoroughly explored for TiB_2, nor has the effect of multiple transition metals on the shell formation being investigated.

Another important characteristic for materials intended for hypersonic systems is ablation resistance. With the aim of decreasing the overall weight without decreasing the ablation performance, partial replacement of ZrB_2 with TiB_2 was identified as a promising approach. The addition of TiB_2 was coupled with the concomitant introduction of another functionalizing TM to compensate for the decrease in oxidation behaviour that accompanies TiO_2 formation. In this respect, CrB_2 was selected based on its oxide's melting point, its capability to promote densification [18] and to increase the hardness of ZrB_2 [8], and its ability to retard oxidation [19,20]. Furthermore, if included in the major boride solid solution, Cr may assume a metallic nature and remain encapsulated in the oxide once the ceramic is exposed to oxidation (Fig. 1) [14].

Aware of issues that can be encountered when trying to dissolve cations with poor solubility into the major boride lattice, we adopted a multi-step high energy milling procedure to favour the formation of $(Zr,Cr)B_2$ solid solution over the formation of $(Ti,Cr)B_2$ one.

Therefore, the purpose of this study was to study the microstructure and local mechanical properties of fully dense ZrB_2–TiB_2 ceramics with Cr additions.
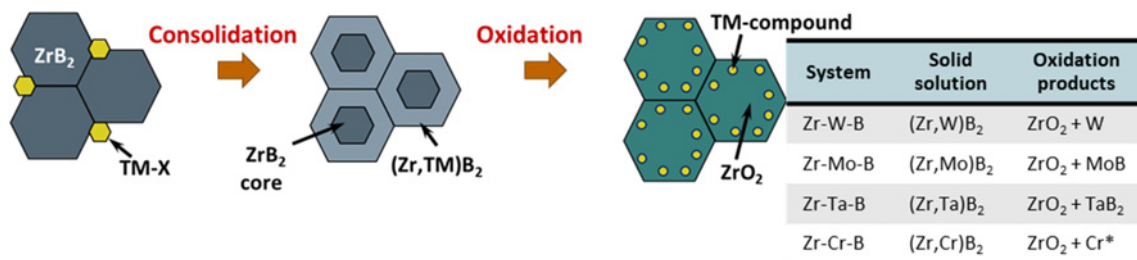

System	Solid solution	Oxidation products
Zr-W-B	$(Zr,W)B_2$	ZrO_2 + W
Zr-Mo-B	$(Zr,Mo)B_2$	ZrO_2 + MoB
Zr-Ta-B	$(Zr,Ta)B_2$	ZrO_2 + TaB$_2$
Zr-Cr-B	$(Zr,Cr)B_2$	ZrO_2 + Cr*

Fig. 1 Sketch of core–shell structure development in ZrB_2 ceramics in presence of a transition metal compound (TM-X) upon consolidation and evolution upon oxidation with the different products experimentally observed or predicted (*) depending on the TM [14–17].

2 Experimental procedure

Commercial powders were used to prepare the ceramics: hexagonal ZrB_2 (H.C. Starck, Germany; Grade B, specific surface area 1.0 m^2/g, particle size range 1.5–3.0 μm, impurity (wt%): C 0.2, O 0.7, N 0.10, Fe 0.1, Hf 1.7); hexagonal TiB_2 (H.C. Starck, Germany; Grade F, particle size range 2.5–3.5 μm, impurity (wt%): C 0.4, O 2.5, N 0.5, Fe 0.1); SiC (H.C. Starck, Germany; Grade BF-12, specific surface area 11–13 m^2/g, mean particle size 0.6 μm); and hexagonal CrB_2 (H.C. Starck, Germany; Grade B, mean particle size 2.0 μm, impurity (wt%): C 0.1, O 0.4, Fe 0.1).

A powder mixture containing 60 vol% ZrB_2, 30 vol% TiB_2, 5 vol% CrB_2, and 5 vol% SiC was prepared by a multi-step dry milling process in a planetary high energy ball mill (HEBM, Retsch PM 100) using Y-stabilized ZrO_2 balls and vessel. After an initial step to physically mix the ZrB_2 and CrB_2 (5 min, ball to powder mass ratio 1 : 20, 200 r/min), the rotation speed was increased to 400 r/min for 25 min to promote the formation of the desired $(Zr,Cr)B_2$ solid solution. Then, TiB_2 powder was added and milled for 10 min with a 1 : 40 ball to powder mass ratio at the same speed. In the last step, SiC was added and milled at lower intensity to avoid its oxidation (5 min, 1 : 20 ball to powder mass ratio, 200 r/min).

The resulting powder mixture was uniaxially pressed into green pellets that were approximately 44 mm in diameter and 10 mm in thickness. The pellets were sintered in mild vacuum (~10 Pa) using an induction-heated graphite hot pressing furnace with different sintering cycles.

The first material, labelled ZTC-A, was densified by heating at 600 ℃/h up to a maximum temperature of 1910 ℃ with an applied load of 40 MPa, which was held for 12 min before switching off the furnace and letting it cool at its natural rate, around 40 ℃/min from 1910 to 1100 ℃. This one-step cycle resulted in a notable silica-glassy phase at the grain junctions; therefore, a different sintering cycle was performed on a second pellet, labelled ZTC-B, to reduce the amount of glassy-phase. For this second material, the temperature was raised to 1650 ℃ under mild vacuum with a 15 MPa load [21]. It remained at this temperature for 30 min and then the load was increased to 40 MPa upon reaching 1910 ℃, then a 12 min dwell followed. Furthermore, to limit possible micro-cracking, a controlled cooling rate of 20 ℃/min was used from 1910 to 1100 ℃ without applied load (Table 1).

For comparison, the same composition was prepared through conventional wet ball milling (WBM) using SiC milling media and ethanol, with equal weight ratio of powder to media to solvent, and 24 h milling time. This mixture, labeled as ZTC-C, was sintered adopting the intermediate hold at 1650 ℃ and slow cooling upon reaching the maximum temperature of 1910 ℃ (Table 1).

Particle size distribution of the as-received single component powders and the milled powder mixtures was examined by laser diffraction particle size analyzer (Mastersizer 2000 Malvern Instruments Ltd.), which covers the 0.02–2000 μm particle size range. For the analysis, the powders were dispersed in distilled water using low intensity ultrasound at a frequency of 40 kHz and power of 50 W for 5 min.

All the ceramic powder mixtures were characterized by X-ray powder diffraction (XRPD) using Ultima IV Rigaku diffractometer, equipped with Cu $K\alpha_{1,2}$ radiation, using a generator voltage of 40.0 kV and a filament current of 40.0 mA. The range of $10°$–$80°$ 2θ was used with a scanning step size of 0.02° and at a scan rate of 5 (°)/min. The instrument was equipped with a D/TeX Ultra high-speed detector. After hot pressing, pellets were analyzed by X-ray diffraction (XRD, mod. D8 Advance - Bruker, Germany).

The density of the sintered specimens was measured using Archimedes' method in distilled water.

Table 1 Powder processing, sintering conditions, experimental density (ρ), mean grain size (m.g.s.), and micro-hardness (HV) of the multi-phase ceramics. HEBM: high energy ball milling, WBM: wet ball milling

Label	Powder processing	Sintering conditions (℃, MPa, min)	Exp. ρ (g/cm³)	m.g.s. (μm)	HV (GPa)
ZTC-A	Dry, planetary HEBM	1910, 40, 12, natural cooling	5.21	ZrB_2: 2.1±0.8	18.9±0.3
				TiB_2: 1.9±0.9	
ZTC-B	Dry, planetary HEBM	1650, 15, 30 & 1910, 40, 12, slow cooling	5.42	ZrB_2: 1.6±0.6	23.8±0.4
				TiB_2: 2.0±0.8	
ZTC-C	Ethanol, conventional WBM	1650, 15, 30 & 1910, 40, 12, slow cooling	5.38	ZrB_2: 1.7±0.5	N.A.
				TiB_2: 2.1±0.9	

The powder morphology and the microstructure of the sintered ceramics were analyzed on polished and fractured surfaces by field-emission scanning electron microscopy (FESEM, ΣIGMA, ZEISS NTS Gmbh, Germany) coupled to energy dispersive X-ray spectroscopy (EDS, mod. INCA Energy 300, Oxford instruments, UK) for chemical analysis. Key microstructural features, like residual porosity, mean grain size, and volumetric content of the secondary phases, were evaluated using computerized image analysis (Image Pro Plus, v.7, Media Cybernetics, USA) of FESEM micrographs.

Further observations by transmission electron microscopy (TEM) were carried out upon preparation of specimens via standard mechanical thinning methods. First, a 3 mm wide disc was cut from the bulk material and mechanically ground down to a thickness of about 80 μm. Then, a 60 μm deep bowl was ground in the center of the disc using a dimpler equipped with a diamond covered wheel leaving the sample at a thickness of 20 μm in the center. The final thinning was performed with an argon Precision Ion Polishing System (PIPS, Gatan 691) until incipient perforation occurred. Local phase analysis was carried out using a TEM (FEI Tecnai F20 ST) with a nominal accelerating voltage of 200 kV and equipped with energy dispersive X-ray system (EDAX EDS PV9761 SUTW). Electron diffraction patterns were resolved through the commercial software JEMS (Java Electron Microscopy Software, P. Stadelmann, Switzerland).

Microhardness measurements were conducted on the polished surface of the ceramics using an indenter (Innovatest Falcon 505) equipped with a Vickers tip using a load of 9.81 N applied for 10 s following the European standard ENV 843-4. At least ten indentations were done on each material.

In addition, nanoindentation tests were carried out on material ZTC-B to characterize the local properties in the various regions of the grains, using two different machines: the nanoindenter XP™ (MTS Systems Corporation, Oak Ridge, TN, USA) and the KLA iMicro nanoindenter (KLA Corp., USA), both equipped with a Berkovich diamond tip. For a direct correlation between position and properties, data from the nanoindenter XP were employed: 150 indentations, arranged in a 10×15 array, were performed with controlled depth of 80 nm and distance of 1 μm one from the other, and then SEM images were captured over the indented area to discriminate the exact position of the nanoindentations and calculate average values for the core and shell phases. Data falling on the grain boundary, pores, or flaws were excluded upon SEM analysis.

Another series of tests were conducted using the high-speed iMicro apparatus to sample a much wider area and obtain maps with 2500 indentations spaced 3 μm performed with 15 mN load, corresponding to around 120–140 nm penetration depth. The data obtained from this larger array were filtered and only values within 10–50 GPa hardness and 300–600 GPa modulus were considered for statistical analyses. The data distribution was deconvoluted using the Gaussian Mixture Model to obtain the properties of the individual phases and estimate their volume fraction.

In both cases, the indenter was continuously loaded up to the peak load with a load rate of $\dot{p}/p = 0.05\ \mathrm{s}^{-1}$ and immediately unloaded with no holding time. Nanohardness and indentation elastic modulus were calculated using Oliver and Pharr's method [22]. Before the tests, the area function of the indenter tip was calibrated on a standard fused silica specimen. For simplicity, a Poisson's ratio of 0.11 was selected for all phases [23].

3   Results and discussion

3.1   Powder mixtures

Dynamic light scattering results in Fig. 2(a) show that both milling routes led to decreased particle sizes, but HEBM was more effective in decreasing the coarse particle volume fraction. In particular, HEBM increased the fraction of particles with sizes around 1–2 μm. Characteristic particle sizes are reported in the table inset in Fig. 2(a). XRD spectra in Fig. 2(b) were similar and did not give evidence of any mechano-chemical reactions: all the starting phases were present after HEBM, with no evidence of solid solution formation, no new phases nor detection of crystalline oxides. The low intensity peaks at 23° and 29° were attributed to a $Na_2Si_2O_5$ compound, due to contamination during analysis. SEM–EDS showed that HEBM produced more rounded powder particles, whereas faceted particles were observed in the WBM powders (Figs. 2(c) and 2(d)). Furthermore, EDS indicated that oxygen contamination increased from 0.7 wt% in the as-received ZrB_2 and 2.5 wt% in the
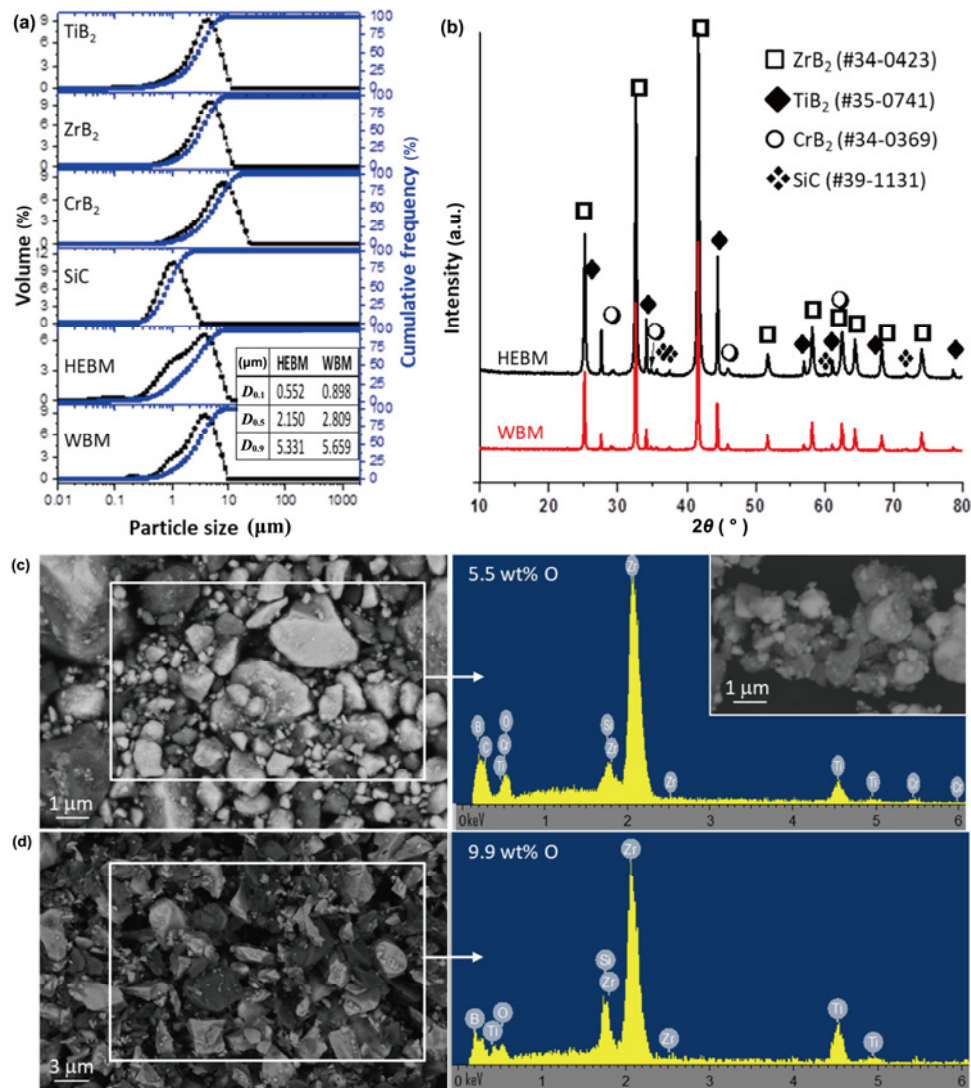
Fig. 2 Characterization of the powder mixtures prepared by planetary high energy ball milling (HEBM) and conventional wet ball milling (WBM): (a) particle size distribution as measured by DLS, (b) X-ray diffraction patterns, and SEM images with EDS spectra showing the overall oxygen contamination (c) in the HEBM mixture and (d) in the WBM mixture.

as-received TiB_2 powders, to 5.5 wt% in the high energy milled powder mixture, and up to 9.9 wt% in the wet ball milled mixture. Since X-ray diffraction did not reveal any oxide attributable to the batched phases, we assume that they were in amount below the detection limit and/or in amorphous state.

3.2 Densification behavior

Figure 3 compares the shrinkage behavior of the powder mixtures prepared by HEBM and WBM. After the dwell period at 1650 ℃ and the application of 40 MPa, a short plateau was measured for both mixtures. The WBM powders started to shrink at 1710 ℃ (onset temperature, T_{on}), which was a lower temperature compared to the HEBM powders that

started to shrink at 1740 ℃. Similarly, the highest densification rate, as determined from the $\Delta\rho/\Delta t$ ratio of the shrinkage curves, was notably higher for the WBM mixture, around 1.2×10^{-3}% s^{-1}, as compared to that measured for the HEBM mixture, around 9.2×10^{-4}% s^{-1}. Both the lower onset temperature for densification and the higher densification rate observed for the WBM powders are presumably due to the presence of higher fraction of oxide-based phases in the WBM powders, which could be in the form of ZrO_2, TiO_2, Cr_2O_3, B_2O_3, or SiO_2. Amongst the possible systems, the B_2O_3–TiO_2 phase diagram predicts the presence of a liquid phase even for very low contents of B_2O_3 [24], which might have remained despite the intermediate dwell at 1650 ℃, and occurs at temperatures compatible with the sintering
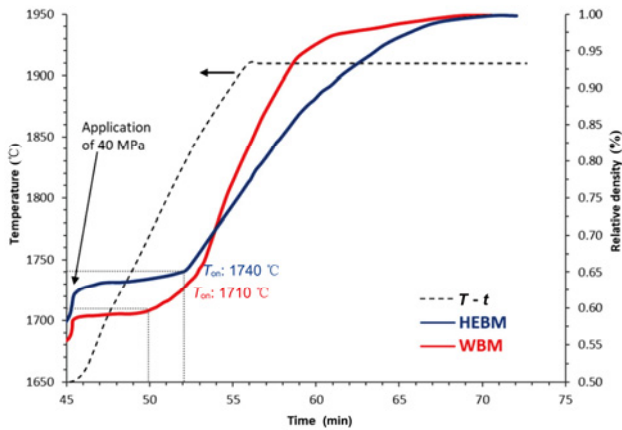
Fig. 3 Densification curves for the mixtures prepared by planetary high energy ball milling (HEBM) and conventional wet ball milling (WBM). Application of mechanical load and shrinkage onset temperatures (T_{on}) are indicated.

schedule adopted. Liquid-phase assisted densification for the WBM mixture is suggested also by the shape of the curve in the final stage of sintering, which is indicated by a sharp shrinkage rate decrease at around 60 min. In contrast, the curve for the HEBM powders follows the typical shape of a solid state sintered ceramic with continuous and slow increase in density.

3.3 X-ray diffraction of the sintered ceramics

XRD of the as-sintered ceramics did not show any significant differences between ceramics produced by the two different sintering cycles or powder milling methods. As a result, only the XRD pattern of ZTC-B is presented in Fig. 4. For all ceramics, the major phase was ZrB_2 with peaks shifted to higher diffraction angles compared to the reference pattern (PDF#34-0423) due the formation of a solid solution with Ti (0.145 nm) and Cr (0.125 nm) that have smaller atomic radius compared to Zr (0.160 nm). The new lattice parameters of the ZrB_2-rich phase were a = 3.1279 Å and c = 3.4396 Å. These lattice parameters would correspond to a composition of $(Zr_{0.7}Ti_{0.3})B_2$ if only Ti had entered the ZrB_2 lattice based on an estimate made using the linear Vegard's rule and the lattice parameters reported for ZrB_2 and TiB_2 (Table 2). Our assumption is further supported by the size factor discussed later in Section 3.5.1.

However, TiB_2 peaks were observed in their reported positions. The most intense peaks, for the (100), (101), and (110) planes, exhibited splitting, suggesting formation of core–shell structures, as highlighted in the inset in Fig. 4. Since these additional
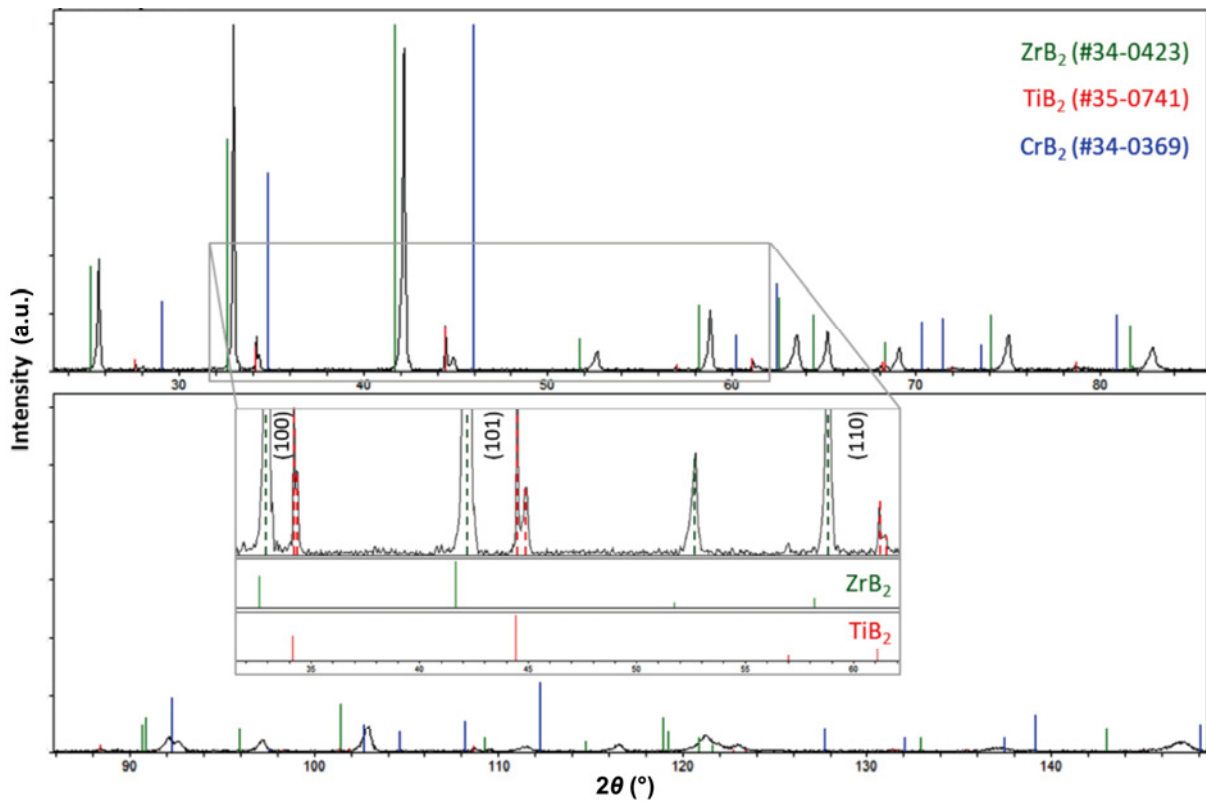

Fig. 4 XRD pattern of the sintered ZrB_2 + 30 TiB_2 + 5 CrB_2 + 5 SiC (ZTC-B) ceramic highlighting ZrB_2 peaks shift and TiB_2 peaks splitting in the inset.

Phase	PDF#	a (Å)	c (Å)
ZrB_2	34-0423	3.169	3.530
TiB_2	35-0741	3.030	3.230
CrB_2	34-0369	2.973	3.071
$(Zr_{0.7}Ti_{0.3})B_2$ replacing ZrB_2	—	3.128	3.439
$(Ti,Cr)B_2$ around TiB_2	—	3.0123	3.2234

TiB_2 peaks were located at higher angles than the theoretical ones (PDF#35-0741), it indicates that this crystalline phase had smaller lattice parameters than nominally pure TiB_2. The shift in lattice parameters also suggested that smaller Cr atoms substituted onto Ti sites in the TiB_2 lattice, since both the atomic radius of Zr and the lattice constants of ZrB_2 are the largest amongst the species involved (Table 2). According to a first estimation using Vegard's rule on the resolvable peaks, the lattice parameters of the new TiB_2-rich solid solution were $a = 3.0126$ Å and $c = 3.2234$ Å. Neglecting any dissolution of Zr into this phase, led to estimate a solid solution with 30 at% Cr, considering the apparent a lattice parameter, but with only 5 at% when the c lattice parameter was considered. Cell anisotropy in TiB_2 is well documented and has

been attributed to the bonding in the lattice [23,25,26]. Specifically, the strong B rings, that are parallel to the a-direction, limit the amount that the a-parameter can change. On the other hand, along the c-direction, the bonds are not under such constraint and the weaker TM-B bonds allow the c-parameter to change by a greater amount [27].

Neither SiC nor CrB_2 were detected by XRD due to the lower scattering efficiency of SiC, and the likely loss of CrB_2 due to solid solution formation.

3.4 Microstructure of the sintered specimens

The bulk densities of the sintered ceramics were 5.21 g/cm³ for ZTC-A, 5.42 g/cm³ for ZTC-B, and 5.38 g/cm³ for ZTC-C and in all cases a porosity below 0.5% was estimated by SEM analysis (Table 1). The lower density of ZTC-A is possibly due to the retention of residual silica with lower density (2.2 g/cm³) compared to the other constituents.

3.4.1 ZTC-A

A low magnification inspection of the ZTC-A material showed that it was almost completely dense and free of macro defects (Fig. 5(a)). However, higher magnification images showed diffuse microcracking. In the ZrB_2-based
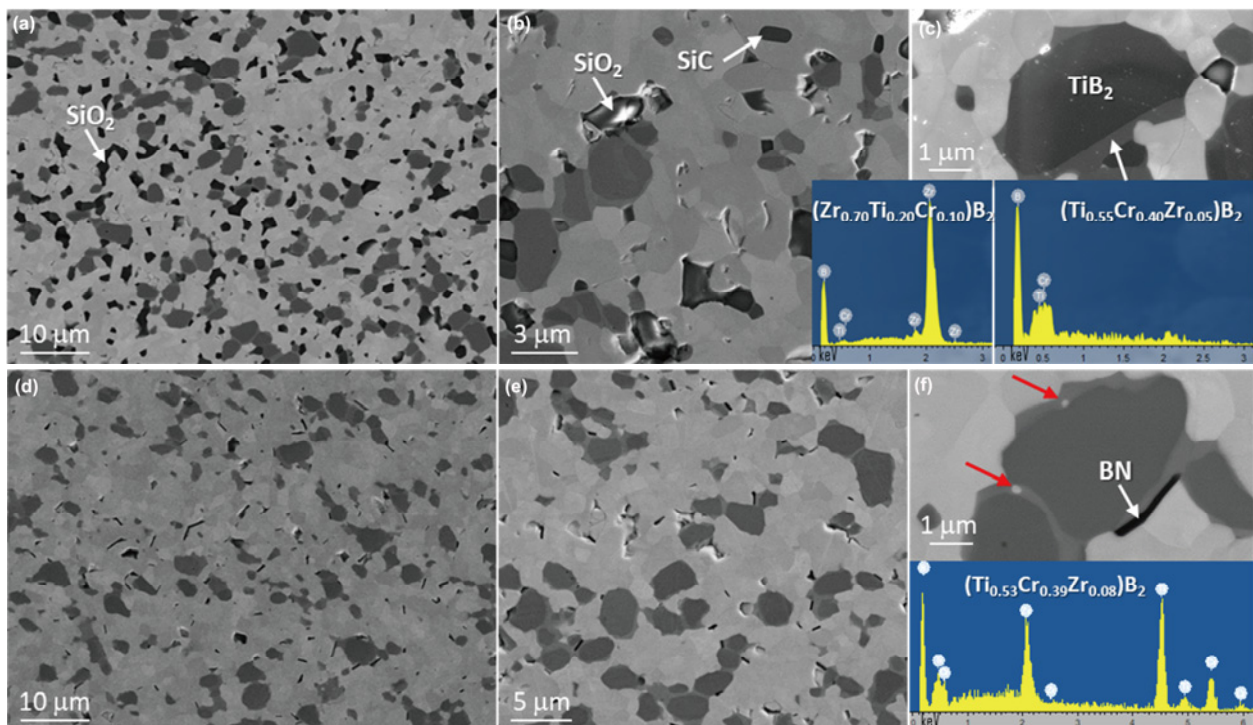

Fig. 5 Representative SEM images of the sintered (a–c) ZTC-A and (d–f) ZTC-B ceramics with corresponding EDS spectra. Red arrows in (f) highlight particles trapped at the TiB_2 core–shell interface.

matrix, which was characterized by a light gray contrast in BSE mode, TiB_2, SiC, and SiO_2 were visible as additional phases. Higher magnification images in Figs. 5(b) and 5(c) highlighted the formation of core–shell structures within TiB_2 grains, being dark-contrasted and composed of pure TiB_2 in the core and a mixed solid solution including Cr and Zr in the shell. A possible composition was estimated by EDS as $(Ti_{0.55}Cr_{0.40}Zr_{0.05})B_2$ (Fig. 5(c)).

Core–shell structures were not observed for ZrB_2-rich grains, which had instead irregular contrasts between inner and outer portions of the grains. Nevertheless, point EDS detected up to 20 at% titanium and about 10 at% chromium in the ZrB_2 grains, suggesting a possible formula of $(Zr_{0.70}Ti_{0.20}Cr_{0.10})B_2$.

No individual CrB_2 grains were found even though 5 vol% CrB_2 was present in the initial batch. This observation implies that Cr completely dissolved into the other boride phases and, based on EDS analysis, preferentially into the shell around TiB_2 grains, with contents up to 40 at%.

Both boride phases had mean grain sizes of around 2.0 μm. In addition, the residual oxide content was around 4 vol% in the form of silica, that likely contributed to incomplete densification (Fig. 5(b) and Table 1). Image analysis also showed about 4 vol% of well dispersed SiC particles and traces of BN phase, which derives from the reaction between boron oxide covering the boride particles and N present as impurity in both ZrB_2 and TiB_2, 0.10 and 0.50 wt%, respectively [28].

3.4.2 ZTC-B

This material was obtained adopting processing strategies designed to decrease the residual oxygen content, promote densification, and mitigate microcracking. First, a dwell at 1650 ℃ was introduced during hot pressing to remove the oxide phases by reactions that form oxygen-containing vapor species. The removal of oxide phases should reduce the driving force for grain coarsening and promote densification [29]. Second, controlled cooling was used from the sintering temperature of 1900 ℃ down to 1100 ℃ to minimize micro-cracking. Among other effects, these changes had a noticeable impact on the hardness, which increased from 18.9±0.3 GPa in ZTC-A to 23.8± 0.4 GPa in ZTC-B (Table 1).

Figures 5(c)–5(f) show the microstructure of the ZTC-B ceramic. The mean grain size of the Zr-rich boride was around 1.6 μm and the grain size of the

Ti-rich boride was around 2.0 μm. Notably, the silica pockets that had been obvious in ZTC-A were not present and microcracking was also eliminated. As with ZTC-A, the ZrB_2 grains in ZTC-B did not show core–shell structures, but appeared to have a homogeneous composition close to $(Zr_{0.74}Ti_{0.20}Cr_{0.06})B_2$, which was in agreement with X-ray diffraction. The composition of the TiB_2 shell was $(Ti_{0.53}Cr_{0.39}Zr_{0.08})B_2$, confirming the preferential dissolution of Cr into the TiB_2 lattice rather than into that of ZrB_2 and in accord with the composition estimated for ZTC-A, within the technique error. In addition, bright particles were often found trapped at the core–shell interface (Fig. 5(f)).

Image analysis revealed around 1 vol% of BN at grain boundaries (Fig. 5(d)). For this ceramic, SiC was rarely found, possibly due to active oxidation occurred during the 1650 ℃ dwell under mild vacuum conditions as explained in Ref. [7].

By studying the SEM images of the polished or fractured surface of ZTC-B, two types of precipitates were observed. A few larger (around 200 nm), rounded precipitates were observed at the TiB_2 core–shell interfaces, as shown by the red arrows in Fig. 6, while other smaller (around 10–30 nm), more numerous precipitates were present in both ZrB_2 and TiB_2 grains as indicated by green arrows in Fig. 6. When precipitates were encountered, the fracture was characterized by cleavage planes, whereas the core remained flatter, as remarked in similar multi-scale textured systems [11,12].

TEM analysis provided further support for the formation of the core–shell structure in the titanium diboride grains, as visible in the overview images of Fig. 7(a). In STEM mode, the dark grains are TiB_2-based, while the bright ones are based on ZrB_2. Electron diffraction patterns of the TiB_2 cores and shells showed epitaxy between the two regions and a core–shell interface characterized by an intricate dislocation network and dislocation tangles that presumably originated due to the different thermal expansion coefficients (Figs. 7(b) and 7(c)). The composition of the shell was estimated to be $(Ti_{0.50}Cr_{0.40}Zr_{0.10})B_2$ by TEM–EDS (Fig. 7(d)), which was very close to that estimated by SEM–EDS (Fig. 5(f)).

Focused analysis by TEM, revealed few larger nano-particles trapped particles at the TiB_2 core–shell interface and within the shell itself. The size of these varied between 50 and 200 nm as shown in Figs. 7(a), 8(a), and 8(b). According to EDS composition profiles and
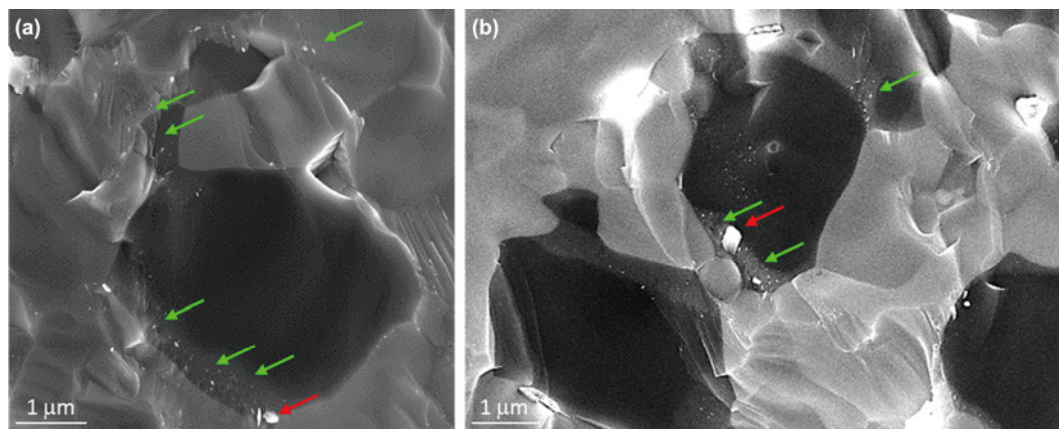
Fig. 6 SEM fracture surfaces of the ZTC-B ceramic showing nanotexturing in the solid solution area. Larger particles are highlighted by red arrows, small ones by green arrows.
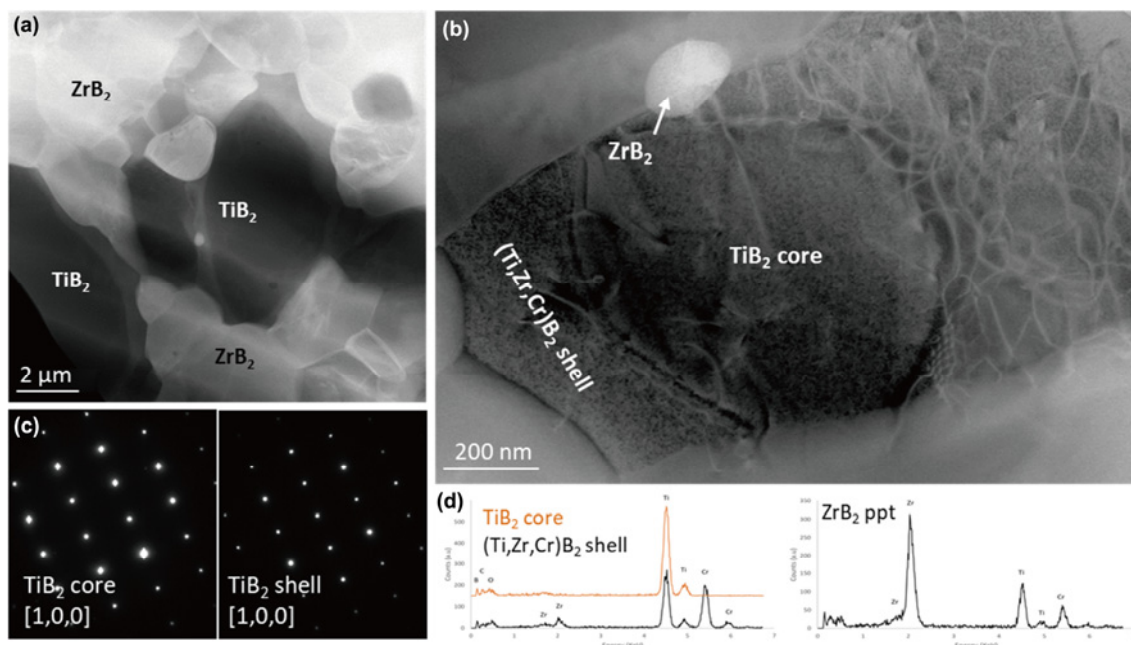

Fig. 7 TEM images of the ZTC-B ceramic showing (a) the microstructure overview, (b) the core–shell outlook in TiB_2 grains featured by epitaxy, bright contrasted polygonised dislocation walls and networks, and a trapped ZrB_2 particulate with corresponding (c) electron diffraction pattern and (d) punctual EDS spectra taken on TiB_2 core, shell and on the white precipitate in (b).

electron diffraction collected on these particles, reported in Figs. 8(c)–8(e), the larger particles appear to be ZrB_2 with clean grain boundaries with the surrounding TiB_2-rich grains (Fig. 8(f)). Judging by their size and their well-nestled position within the TiB_2-rich grains, they are presumed to have precipitated from the super-saturated $(Ti,Zr,Cr)B_2$ solid solution shell. However, they could also be ZrB_2 fragments that remained trapped during grinding, especially those located at the shell–shell interfaces.

Regarding the nano-texturing visible by SEM on the fracture surfaces, the presence of tiny precipitates

could not be ultimately confirmed, but they were observed in STEM mode, as shown by the green arrows in Fig. 9.

The TiB_2 grains thinned preferentially during Ar milling. As a result, ZrB_2 grains could not be fully resolved in the TEM specimens produced as part of the present study. ZrB_2 grains appeared brighter and more uniform (Fig. 10(a)). Dislocations in the outer region of the grain might suggest a core–shell structure (Fig. 10(c)). Particles about 50 nm in diameter were commonly found inside ZrB_2 grains, where dislocation networks accumulated, as the inset
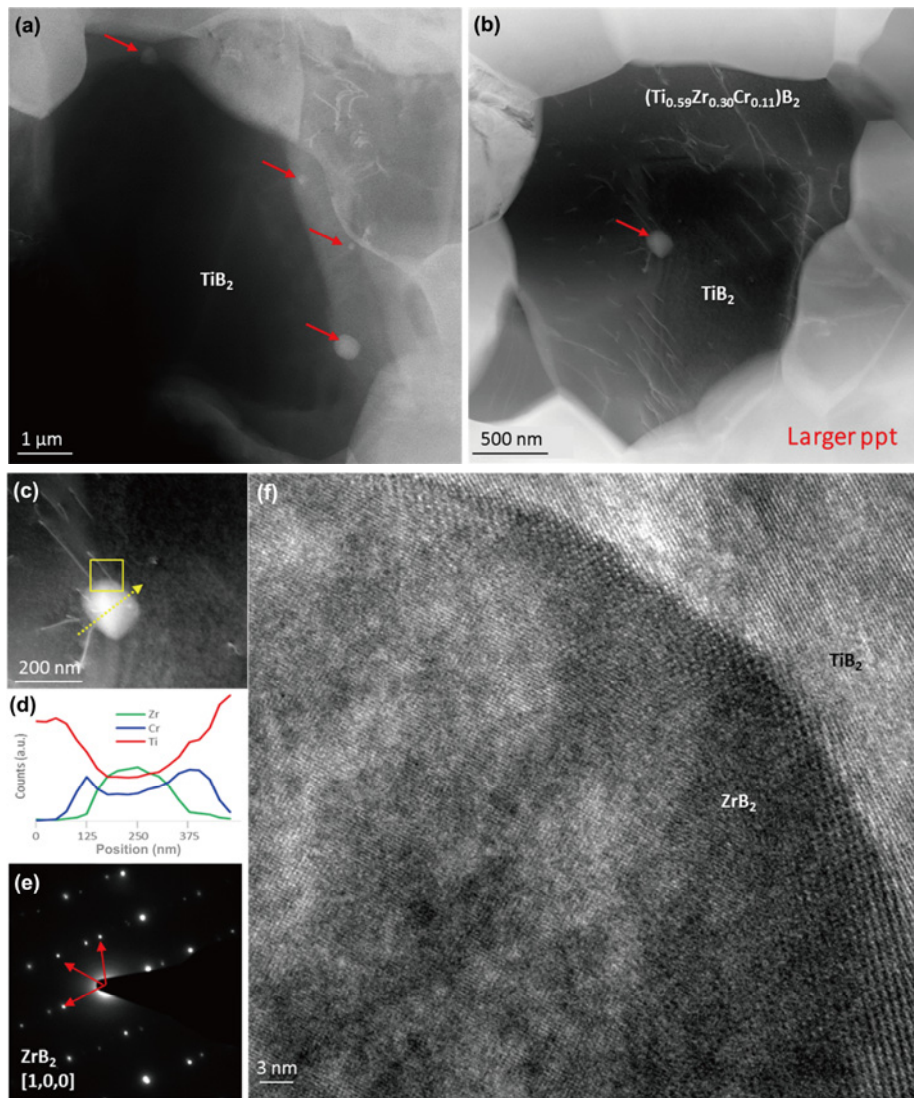
Fig. 8 (a, b) TEM images of ZTC-B highlighting a "large" trapped particle with corresponding magnified image in (c), linear EDS spectra in (d), electron diffraction pattern in (e) pointing to ZrB_2 as most probable compound and (f) HR-TEM image of the inclusions showing clean interfaces between the borides.
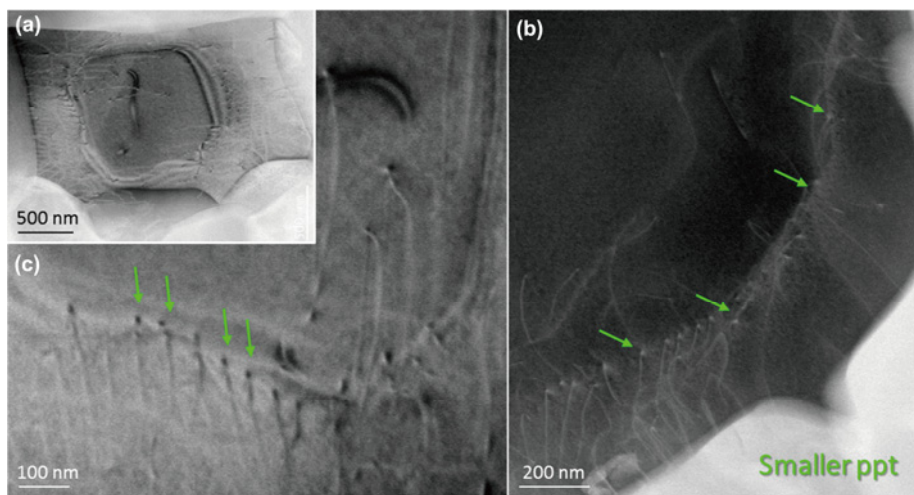

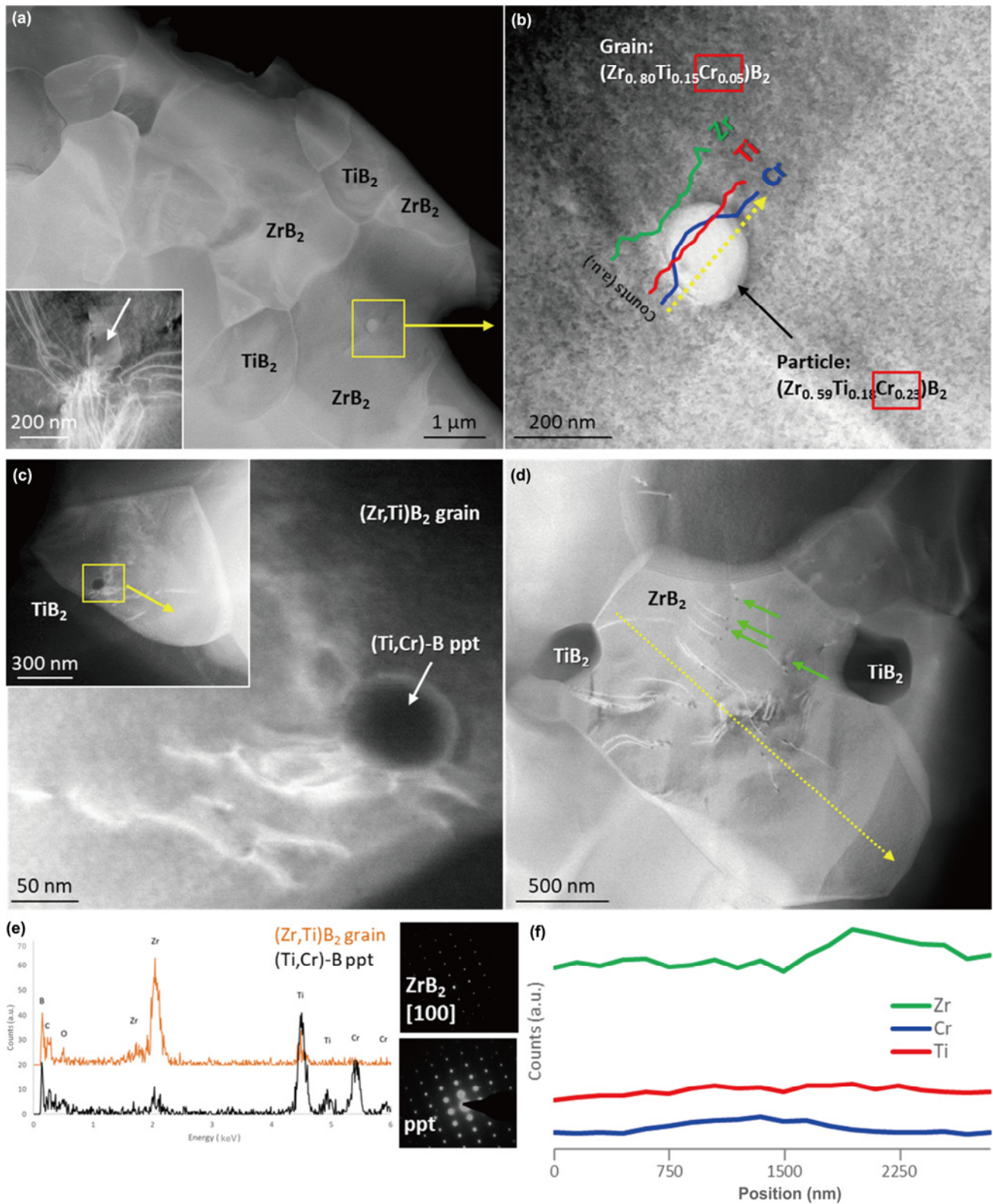**Fig. 9** TEM images of ZTC-B with arrows showing nano-precipitates at the core–shell interface in TiB_2 grains.

Fig. 10 TEM images of ZTC-B showing (a) an overview of ZrB_2 grains with a trapped particle with (b) corresponding linear EDS spectra overlapped, (c) another trapped inclusion at low and high magnification with (e) point EDS detecting Cr enrichment and diffraction patterns taken on ZrB_2 and the precipitate. The inset in (a) highlights the dislocation networks around the nanoparticle. (d) Overview of a ZrB_2 grain highlighting tiny dark precipitates by green arrows and (f) EDS profile scan showing no appreciable cation content variation across the whole grain.

of Fig. 10(a) shows. EDS line scans across these inclusions detected higher amounts of Cr compared to the surrounding matrix, as shown in Figs. 10(b) and 10(c). Dislocations emanated from such inclusions (Fig. 10(c)), but Cr enrichment could only be assessed by point EDS as electron diffraction was not conclusive in resolving the nature of such particles (Fig. 10(e)). Hence, the core–shell feature of ZrB_2 grains could not be confirmed due to questions about its fine structure and composition. In the present case, the contrast variations in ZrB_2 grains are more likely due to thickness effects rather than to composition changes, as suggested by EDS line scans across ZrB_2-rich grains, which gave an average composition close to $(Zr_{0.80}Ti_{0.15}Cr_{0.05})B_2$ (Figs. 10(d) and 10(f)). Also the ZrB_2 grains appeared to have a few of nano-sized precipitates, as pointed by green arrows in Fig. 10(d).

3.5 Solid solution formation in presence of competing TMs

The constituent diborides form partial or complete solid solutions with each other [30,31]. Specifically, the solubility between ZrB_2 and TiB_2 is reported to be continuous, although phase separation has been reported in some cases. In the ZrB_2–CrB_2 system, negligible solubility was reported due to the large difference in lattice constants [32]. Lastly, previous studies on the TiB_2 and CrB_2 mixtures showed complete solubility above 2000 ℃, but a miscibility gap at lower temperatures. Below 1800 ℃, the maximum CrB_2 solubility in TiB_2 was reported not to exceed 1 mol% [33–35]. Recently, complete solid solubility in a $(Ti_{0.9}Cr_{0.1})B_2$ powder was achieved already upon boro/carbothermal reduction synthesis at 1650 ℃ followed by consolidation by spark plasma sintering at 2000 ℃ [8].

To better understand the solubility in these complex systems, a summary of the composition of the solid solutions detected around TiB_2 grains or in place of ZrB_2 in the ZTC-B ceramic is reported in Table 3, where a good agreement amongst XRD, SEM–, and TEM–EDS can be assessed except for the TiB_2 solid

solution that displays lattice anysotropy and, as such, the XRD technique should not be considered as the most reliable. In addition, the main features of the ZTC-B ceramic are summarized in the following:

- CrB_2 was not found as a separate phase in the sintered ceramic and Cr preferably dissolved into TiB_2 (40 at% by TEM) rather than into ZrB_2 (5 at% by TEM).
- ZrB_2 appeared to have a constant composition across its grains, whereas TiB_2 grains clearly displayed core–shell structures.
- While the centers, or cores, of the diboride grains were free of inclusions, two types of nano-inclusions were observed in both Zr- and Ti-B_2 grains: around 200 nm large, visible also on polished cross section, and tiny 10–30 nm ones, appreciable only upon investigation of the fractured surface and barely by TEM.
- The larger inclusions found within TiB_2 grains were identified as a ZrB_2-rich phase; the larger inclusions found within ZrB_2 grains revealed to be multi-phase Cr-rich particles.
- No information is available at this time on the nature of the 10–30 nm inclusions.

Hence, ZTC-B was a complex ceramic system containing two main solid solution phases.

3.5.1 Crystallographic considerations

Atomic size and crystal structure are the primary factors affecting solid solution. The diboride compounds have the same AlB_2 crystal structure, and all cations are introduced in the system as TMB_2 compounds in the AlB_2 structure, with lattice parameters reported in Table 2. According to the Hume–Rothery's rule, if a solute differs in its atomic size by more than 15% from the host, then it is likely to have a low solubility, i.e., the "size factor" is said to be unfavorable. For size differences of less than 15%, TMs should be co-soluble with solute species having a larger atomic radius than the host solute atoms producing a compressive strain in the host lattice, whereas smaller solute species would produce a tensile strain (Fig. 11(a)). The reported

Table 3 Composition of the $(Zr,Cr)B_2$ solid solutions as measured by XRD, SEM, and TEM–EDS

Solid solution (shell)	XRD	SEM–EDS	TEM–EDS
ZrB_2-rich	$(Zr_{0.70}Ti_{0.30})B_2$	$(Zr_{0.74}Ti_{0.20}Cr_{0.06})B_2$	$(Zr_{0.80}Ti_{0.15}Cr_{0.05})B_2$
TiB_2-rich	*a*-axis: $(Ti_{0.70}Cr_{0.30})B_2$ *c*-axis: $(Ti_{0.95}Cr_{0.05})B_2$	$(Ti_{0.53}Cr_{0.39}Zr_{0.08})B_2$	$(Ti_{0.50}Cr_{0.40}Zr_{0.10})B_2$

atomic radii of the species involved are 0.145 nm for Ti, 0.160 nm for Zr, and 0.125 nm for Cr. Substitution of either Cr or Ti into the ZrB_2 lattice causes tension state of the lattice. In contrast, dissolving Zr into TiB_2 would cause compression whereas substitution with Cr would cause tension. Furthermore, considering substitution into ZrB_2, Ti has a difference of 9.4% compared to a size difference of 21.9% for Cr, which is consistent with the observed formation of $(Zr,Ti)B_2$ solutions rather than $(Zr,Cr)B_2$. Based on this assessment, even though the mixing procedure was designed to promote Cr dissolution into ZrB_2, $(Ti,Cr)B_2$ formed preferentially at the end. On the other hand, both Cr and Zr dissolved into TiB_2 based on size differences of 10.3% with Zr and 13.8% with Cr. The plots in Fig. 11(b) show the difference in percentage, amongst the atomic radii of the involved transition metals and amongst the corresponding borides cell volumes. Considering the volume cell parameters, according to the 15% rule, while assessing the unfavorability of $(Zr,Cr)B_2$, also the formation of $(Zr,Ti)B_2$ or the opposite $(Ti,Zr)B_2$ should not be favorable. In contrast, $(Ti,Cr)B_2$ is favorable considering both the atomic radii of the TM and the borides cell volumes.

These guidelines also suggest an explanation for the formation of the precipitates within the main boride grains, which is sketched in Fig. 11(c). If these precipitates formed *in situ* during sintering, Cr-rich particles within $(Zr,Ti)B_2$ grains suggest that the solid

solubility of Cr in ZrB_2 lattice was achieved at the densification temperature and upon cooling, the new crystalline CrB_2 phase preferably precipitated. However, TiB_2-based grains present a less-consistent situation. The ZrB_2 precipitates in TiB_2, shown in Fig. 8 and sketched in Fig. 11(c), appear to contradict the atomic radius size-driven precipitation since the size difference between Cr and Ti is greater. However, the volume cell of TiB_2 and CrB_2 are closer than those of ZrB_2 and TiB_2 (Fig. 11(b)), which may have been the deciding factor in the stability of the solid solutions.

3.5.2   Thermodynamic considerations

Previous investigations on similar solid solutions involving only two cations revealed that the nature of the inclusions differed depending on the TM. When W was introduced into a ZrB_2 system, round W nanoinclusions precipitated from a super-saturated $(Zr,W)B_2$ solid solution. In contrast, when Ta was added, TaC nano-laths formed from the analogous $(Zr,Ta)B_2$ solid solution [12]. The formation of metal or carbide was attributed to the reaction of the metal (W or Ta) within the local environment in the furnace, which had low oxygen and CO partial pressures. However, in a study on a W-ZrB_2 alloy consolidated by SPS at 1600 ℃, it was shown that the boride reacted with C and O to form multiple second phases with different crystal structures, including ZrO_2 and $ZrC_{0.7}$ [36], thus putting forward
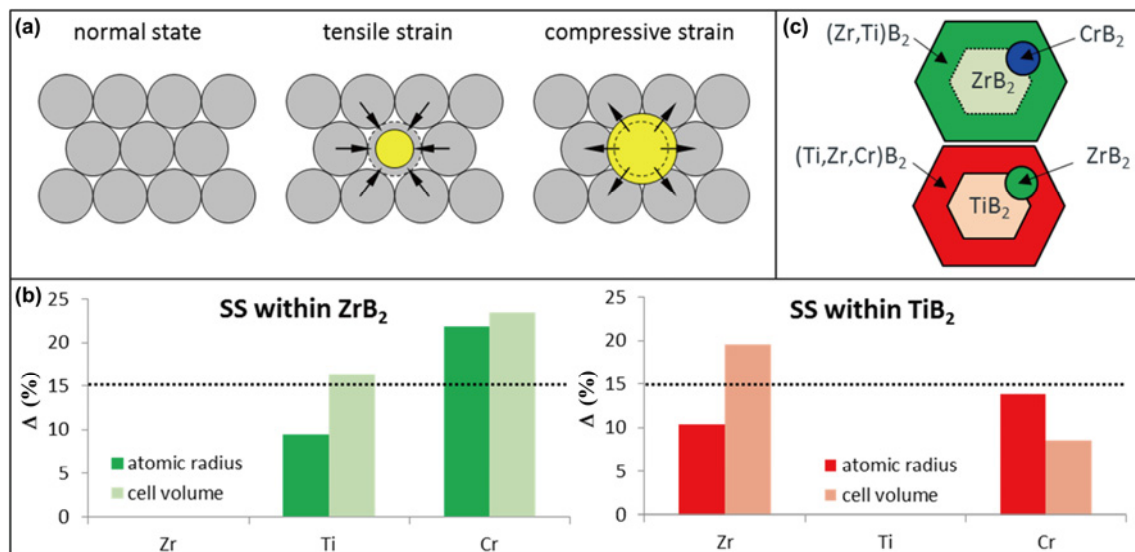

Fig. 11 (a) Local stress in substitutional solid solutions induced in the host cell in the case of incorporation of smaller or larger species (yellow spheres). (b) Plot of the difference amongst Ti, Zr, Cr atomic radius and amongst the corresponding boride cell volume; a value below 15% indicates favourable tendency to form solid solution within ZrB_2 or TiB_2 lattice. (c) Sketch of the ZrB_2- and TiB_2-rich grains asset upon sintering.

the strong influence of the sintering environment and powder impurities as promoter of the formation of one or another compound.

In the present work, the precipitating phases were borides, which could be due to the higher content of boride phase, 95 vol% of $ZrB_2 + TiB_2 + CrB_2$, in the nominal powder mixtures. The powders also contained oxygen impurities, which were present in the as-supplied powders and further additionally introduced by milling in air. The B-rich environment might have resulted in favorable conditions for precipitation of borides instead of carbides or metal. To define which is the most favorable gaseous B-phase developed upon hot pressing of our ceramics, a commercial software package (HSC Chemistry for Windows 5, Outokumpu Research Oy, Pori, Finland) was employed and run from room temperature to 2000 ℃ under a pressure of 10 Pa, that is the vacuum level inside the hot-press chamber. For simplicity, ZrB_2 was first considered covered by its natural B_2O_3 in CO environment, with the activity of each phase equal to one. The results of this thermodynamic computation are visualized in Fig. 12(a). The simulations indicate that liquid B_2O_3 vaporizes at around 900 ℃ in the form of B_2O_2 first, with relevant formation of B_2O_3 only above 1100 ℃. B_2O_2 remains the dominant gaseous B-rich phase up to around 1670 ℃, and then, BO prevails until the end of

the sintering. Gaseous B_2O, BO_2, and B start to be developed at around 1400, 1500, and 1700 ℃ respectively, but their content remains however negligible, as highlighted in the magnified region of Fig. 12(a)(bottom).

Next, predominance diagrams in the Zr–B–O and Cr–B–O systems were calculated with the same software at 1900 ℃ and showed that ZrB_2 and CrB_2 are preferred over the corresponding metal or oxide for oxygen partial pressure below 10^{-10} bar and BO partial pressure above 10^{-6} bar (Fig. 13). Cleaning of the sintering environment with further addition of reducing species might change the overall atmosphere conditions to promote precipitation of metallic Zr into TiB_2 and Cr into ZrB_2, leading to consequent benefits on the high temperature properties owing to the metal ductile behavior.

Another interesting finding upon running the equilibrium composition, but using TiB_2 or CrB_2 (Figs. 12(b) and 12(c), respectively), regards the development of metallic Cr in relevant amount already at 1000–1200 ℃, and of metallic Ti above 1600 ℃, whereas in the case of ZrB_2, metallic Zr starts to be released only above 1800 ℃ and in very negligible amount (see the magnified region of Fig. 12(a)(bottom)). This would explain the disappearance of the CrB_2 phase and higher mobility of Cr and Ti over Zr.
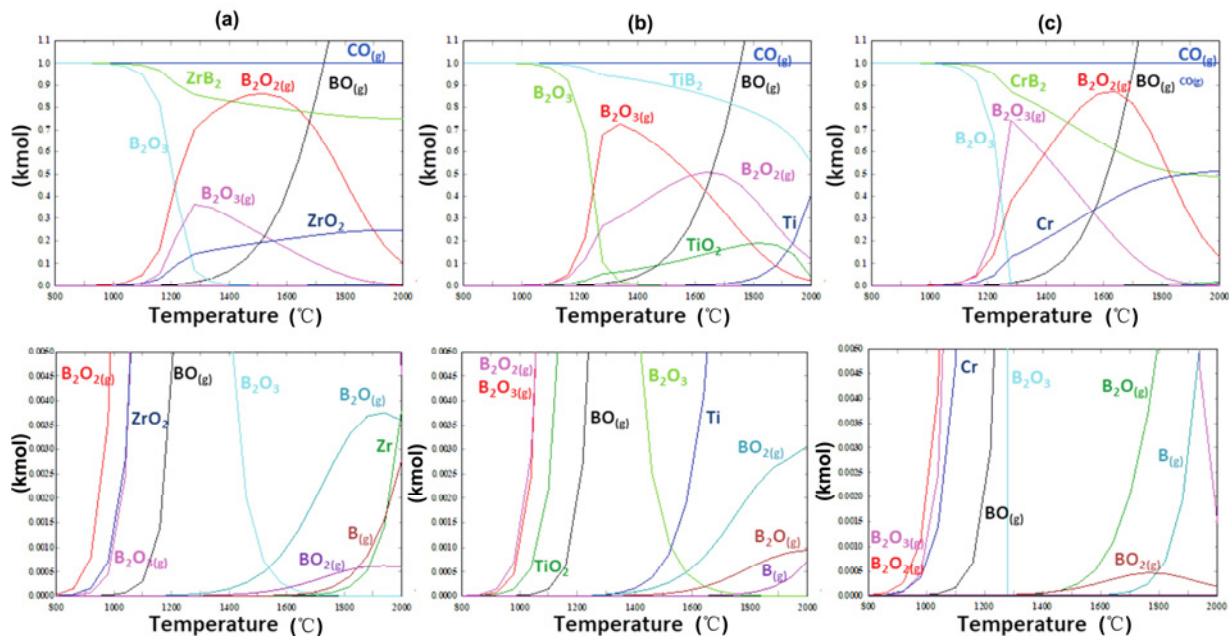

Fig. 12 Thermochemical equilibria of the products deriving from the reaction $TMB_2 + 1CO_{(g)} + 1B_2O_{3(g)}$, with TM = Zr (a), Ti (b), and Cr (c), as a function of the temperature and at constant pressure of 10^{-4} bar. In the bottom, a zoomed portion of the plots above highlights minor gaseous products and different amounts of released TM: relevant in the case of Cr, Ti, and negligible in the case of Zr.
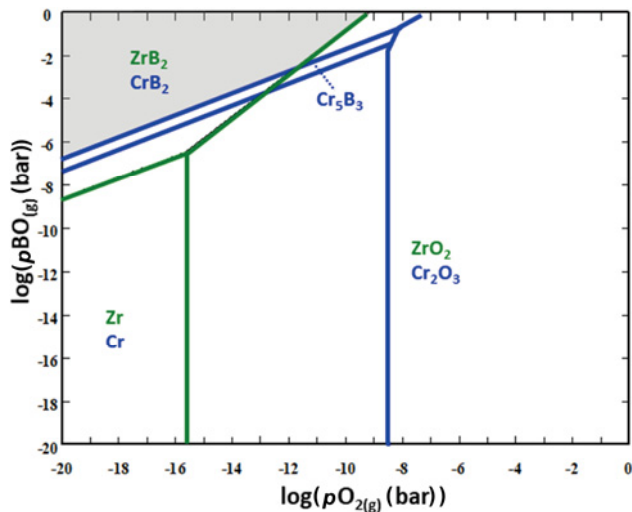
Fig. 13 Predominance stability diagrams for the Zr–B–O and Cr–B–O systems at 1900 ℃ highlighting in grey shaded area the partial pressure conditions within the hot press chamber that yield precipitation of borides into the matrix grains.

3.6 Nanoindentation

A portion of the indentation map performed to a depth of 80 nm (~5 mN) on ZTC-B is depicted in Fig. 14(a),

where TiB$_2$ core and its shell are clearly identifiable, whereas ZrB$_2$ grains appear more homogeneous and therefore measured as a whole. The pure TiB$_2$ resulted the hardest, around 43 GPa, followed by its solid solution, close to 40 GPa, and well above ZrB$_2$ grains, around 36 GPa (Fig. 14(b)). The same trend was observed for the modulus, even if the differences were less marked and a statistical variation between the values of the individual phases is debateable.

A softer shell around TiB$_2$ was already found when it hosted W in its solid solution [37], and could be related to the easiest glide of slip planes due to the presence of nano-inclusions, as suggested by the cleavage fracture of the shell (Fig. 6).

Figures 14(c) and 14(d) present hardness and modulus contour maps for indents at a constant load of 15 mN with the corresponding filtered data and deconvoluted gaussians curves. Deconvolutions were done imposing either two or three peaks, but according to the Akaike Information Criterion (AIC), which is an estimator of the relative quality of statistical models, the three peaks fitting was more appropriate for both hardness and modulus. The hardness and modulus values
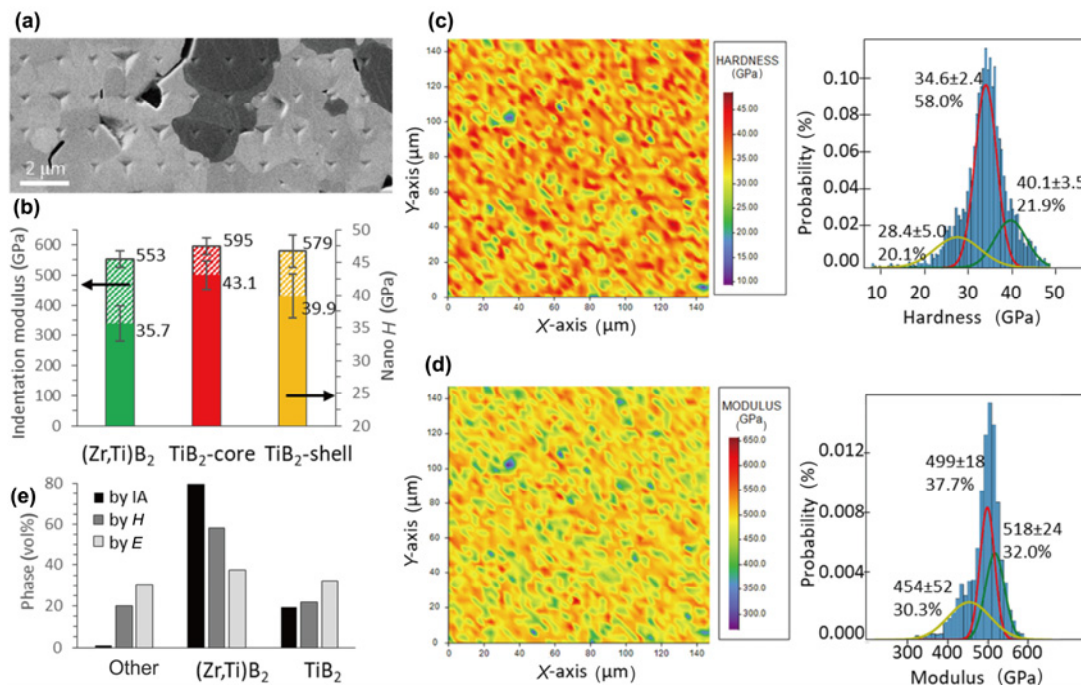

Fig. 14 (a) Portion of a nanoindentation array as viewed by SEM and (b) corresponding hardness and modulus obtained on material ZTC-B with the XP nanoindenter at 80 nm controlled penetration depth. (c) Hardness and (d) modulus maps with corresponding mechanical property histograms overlapped to the deconvolution curves determined by iMicro nanoindenter at 15 mN controlled load (values of hardness or modulus of each distinguished phase are reported on the histograms together with the calculated phase content). (e) Comparisons of the phase volume fraction obtained by image analysis (IA), nanohardness (*H*), and modulus (*E*) from (c) and (d).

were lower than those obtained for the constant depth indentations due to the indentation size effect, since a higher load applied was applied for the constant depth indentation to limit the amount of invalid elastic indentations (15 mN in Fig. 14(b) vs. ~5 mN in Figs. 14(c) and 14(d)).

By deconvolution of the raw data of both mechanical properties, three distinct phases were identified. In addition, their relative amounts were extracted and plotted in Fig. 14(e), where the phase volume fractions of $(Zr,Ti)B_2$, TiB_2-based grains, and other minor phases measured by image analysis (IA) are reported for comparison. IA is given as the most reliable measure of the actual phase content: 79.7 vol% $(Zr,Ti)B_2$ grains, 19.3 vol% TiB_2-rich grains, mostly equally occupied by core and shell regions, and 1.0 vol% of BN phase.

The TiB_2-based grains were the hardest (~40 GPa) and stiffest (~518 GPa) phase with contents varying from 22 vol% based on the hardness map to 32 vol% from the modulus map. As expected, better agreement was obtained between image analysis and hardness, since hardness is a local property. In contrast, modulus is a long-range property and its measurement is influenced by the surrounding phases to a larger extent than hardness. As a result, discriminating local properties, and therefore determining phase fractions, is less accurate when mapping modulus, especially when the values are similar for the constituent phases. No TiB_2-core and TiB_2-shell could be separated by this method. The most predominant phase was attributed to ZrB_2-based grains, with hardness around 35 GPa and modulus around 500 GPa. However, the phase content estimated by the curves was about 58 or 38 vol%, which was not close to the value of 80 vol% determined by image analysis, see $(Zr,Ti)B_2$ in Fig. 14(e). Similarly, the amount of the softest phase determined by indentation did not match with the content of the compounds identified by image analysis. These lowest peaks are thought to be the fraction of $(Zr,Ti)B_2$ matrix affected by the very soft BN phase. While deconvolution of indentation maps may describe the properties and phase fractions for materials constituted by phases with very large properties difference, i.e., WC-Co materials [38,39], this method is not suitable for refinement of local properties in boride systems with similar properties, which means that post-indentation SEM analysis is required.

4　Conclusions

A multi-phase ceramic was produced by hot pressing a mixture of ZrB_2, TiB_2, CrB_2, and SiC. TiB_2 was added to the ZrB_2 matrix to decrease the overall density. A small amount of CrB_2 was added to improve hardness and SiC was added to improve oxidation resistance. CrB_2 was also selected to explore the effect of competing cations on the formation of solid solutions around the native boride grains upon sintering.

Two different sintering cycles and powder processing methods were used. The first hot press cycle ramped directly to the densification temperature, but resulted in microcracking and retention of silica in the ceramic. A revised sintering process included a dwell at 1650 ℃ and slow cooling, which enabled removal of oxides, attainment of full density, and suppression of microcracking. Powder milling by dry planetary high energy milling was more efficient at particle size reduction and resulted in lower quantities of oxide impurities than conventional wet ball milling.

After sintering, complex solid solutions featured by nanotexturing were found within micron-sized boride grains. CrB_2 was not present as a separate phase, but had mostly dissolved into TiB_2 grains, which displayed a core–shell structure. Shells on TiB_2 grains contained up to 40 at% Cr and 10 at% Zr. ZrB_2 grains did not appear to have a core–shell morphology and contained about 20 at% Ti with negligible Cr content. Two types of inclusions were found in boride grains. One type was below 50 nm in diameter and remained unidentified, while the other type was as large as 200 nm. The latter types were ZrB_2 inclusions that precipitated within TiB_2-rich grains, whereas CrB_2 particles preferably precipitated within ZrB_2-rich grains.

Thermodynamics explained the preferential formation of boride inclusions due to the specific sintering atmosphere. Whereas atomic size factors were conducive to elucidate the precipitation of CrB_2 nano-particles into ZrB_2-rich grains and of ZrB_2 nano-particles into TiB_2-rich grains.

Nanoindentation was employed to measure the local hardness and modulus of the various phases. Coupling of an indentation map to SEM analysis enabled identification of TiB_2 grain cores as the hardest and stiffest phase whereas TiB_2-shells and ZrB_2-rich grains were softer. On the other hand, statistical analyses using larger indentation maps were not fully conclusive for an accurate estimation of the phase properties and content.

Therefore, the use of high energy ball milling and the isothermal dwell in the hot pressing cycle yielded a fully dense nano-textured ceramic that had a theoretical density below 6 g/cm^3, and constituent phases with hardness ranging from 36 to 43 GPa. Further investigations will focus on the suitability of this ceramic for hypersonic in terms of mechanical properties and oxidation behavior.

Acknowledgements

Declaration of competing interest

The authors have no competing interests to declare that are relevant to the content of this article.

References

[1] Fahrenholtz WG, Wuchina EJ, Lee WE, *et al*. *Ultra-High Temperature Ceramics: Materials for Extreme Environment Applications*. Hoboken, NJ, USA: John Wiley & Sons, Inc., 2014.

[2] Guo SQ. Densification of ZrB$_2$-based composites and their mechanical and physical properties: A review. *J Eur Ceram Soc* 2009, **29**: 995–1011.

[3] Golla BR, Bhandari T, Mukhopadhyay A, *et al*. Titanium diboride. In: *Ultra-High Temperature Ceramics*. Hoboken, NJ, USA: John Wiley & Sons, Inc., 2014: 316–360.

[4] Wuchina E, Opila E, Opeka M, *et al*. UHTCs: Ultra-high temperature ceramic materials for extreme environment applications. *Electrochem Soc Interface* 2007, **16**: 30–36.

[5] Savino R, Mungiguerra S, Di Martino GD. Testing ultra-high-temperature ceramics for thermal protection and rocket applications. *Adv Appl Ceram* 2018, **117**: s9–s18.

[6] Ping H, Wang GL, Zhi W. Oxidation mechanism and resistance of ZrB$_2$–SiC composites. *Corros Sci* 2009, **51**: 2724–2732.

[7] Fahrenholtz WG. Thermodynamic analysis of ZrB$_2$–SiC oxidation: Formation of a SiC-depleted region. *J Am Ceram Soc* 2007, **90**: 143–148.

[8] Feng L, Fahrenholtz WG, Hilmas GE, *et al*. Superhard single-phase (Ti,Cr)B$_2$ ceramics. *J Am Ceram Soc* 2022, **105**: 5032–5038.

[9] Feng L, Monteverde F, Fahrenholtz WG, *et al*. Superhard high-entropy AlB$_2$-type diboride ceramics. *Scripta Mater* 2021, **199**: 113855.

[10] Silvestroni L, Kleebe HJ, Fahrenholtz WG, *et al*. Super-strong materials for temperatures exceeding 2000 ℃. *Sci Rep* 2017, **7**: 40730.

[11] Silvestroni L, Gilli N, Migliori A, *et al*. A simple route to fabricate strong boride hierarchical composites for use at ultra-high temperature. *Compos B Eng* 2020, **183**: 107618.

[12] Gilli N, Watts J, Fahrenholtz WG, *et al*. Design of ultra-high temperature ceramic nano-composites from multi-scale length microstructure approach. *Compos B Eng* 2021, **226**: 109344.

[13] Silvestroni L, Failla S, Vinokurov V, *et al*. Core–shell structure: An effective feature for strengthening ZrB$_2$ ceramics. *Scripta Mater* 2019, **160**: 1–4.

[14] Silvestroni L, Stricker K, Sciti D, *et al*. Understanding the oxidation behavior of a ZrB$_2$–MoSi$_2$ composite at ultra-high temperatures. *Acta Mater* 2018, **151**: 216–228.

[15] Silvestroni L, Kleebe HJ. Critical oxidation behavior of Ta-containing ZrB$_2$ composites in the 1500–1650 ℃ temperature range. *J Eur Ceram Soc* 2017, **37**: 1899–1908.

[16] Silvestroni L, Sciti D, Monteverde F, *et al*. Microstructure evolution of a W-doped ZrB$_2$ ceramic upon high-temperature oxidation. *J Am Ceram Soc* 2017, **100**: 1760–1772.

[17] Silvestroni L, Mungiguerra S, Sciti D, *et al*. Effect of hypersonic flow chemical composition on the oxidation behavior of a super-strong UHTC. *Corros Sci* 2019, **159**: 108125.

[18] Bannykh D, Utkin A, Baklanova N. The peculiarities in oxidation behavior of the ZrB$_2$–SiC ceramics with chromium additive. *Int J Refract Met Hard Mater* 2019, **84**: 105023.

[19] Grigoriev O, Neshpor I, Vedel D, *et al*. Influence of chromium diboride on the oxidation resistance of ZrB$_2$–MoSi$_2$ and ZrB$_2$–SiC ceramics. *J Eur Ceram Soc* 2021, **41**: 2207–2214.

[20] Murthy TSRC, Sonber JK, Subramanian C, *et al*. Effect of CrB$_2$ addition on densification, properties and oxidation resistance of TiB$_2$. *Int J Refract Met Hard Mater* 2009, **27**: 976–984.

[21] Harrington GJK, Hilmas GE, Fahrenholtz WG. Effect of carbon and oxygen on the densification and microstructure of hot pressed zirconium diboride. *J Am Ceram Soc* 2013, **96**: 3622–3630.

[22] Oliver WC, Pharr GM. An improved technique for determining hardness and elastic modulus using load and displacement sensing indentation experiments. *J Mater Res* 1992, **7**: 1564–1583.

[23] Spoor PS, Maynard JD, Pan MJ, *et al*. Elastic constants and crystal anisotropy of titanium diboride. *Appl Phys Lett* 1997, **70**: 1959–1961.

[24] Pavlikov VN, Yurchenko VA, Tresvyatskii SG. Fig. 06456—System B_2O_3–TiO_2. *Russ J Inorg Chem* 1976, **21**: 233–236.

[25] Munro RG. Material properties of titanium diboride. *J Res Natl Inst Stand Technol* 2000, **105**: 709–720.

[26] Okamoto NL, Kusakari M, Tanaka K, *et al*. Anisotropic elastic constants and thermal expansivities in monocrystal CrB_2, TiB_2, and ZrB_2. *Acta Mater* 2010, **58**: 76–84.

[27] Smith SMI, Feng L, Fahrenholtz WG, *et al*. Thermal and electrical properties of spark plasma sintered $(Ti,Cr)B_2$ ceramics. *J Am Ceram Soc* 2023, **106**: 632–638.

[28] Sciti D, Silvestroni L, Medri V, *et al*. Sintering and densification mechanisms of ultra-high temperature ceramics. In: *Ultra-High Temperature Ceramics*. Hoboken, NJ, USA: John Wiley & Sons, Inc., 2014: 112–143.

[29] Fahrenholtz WG, Hilmas GE, Zhang SC, *et al*. Pressureless sintering of zirconium diboride: Particle size and additive effects. *J Am Ceram Soc* 2008, **91**: 1398–1404.

[30] Villars P, Prince A, Okamoto H. ASM International, Ohio.

[31] Post B, Glaser FW, Moskowitz D. Transition metal diborides. *Acta Metall* 1954, **2**: 20–25.

[32] Otani S, Aizawa T, Kieda N. Solid solution ranges of zirconium diboride with other refractory diborides: HfB_2, TiB_2, TaB_2, NbB_2 and CrB_2. *J Alloys Compd* 2009, **475**: 273–275.

[33] Fotsing ER. Phase transformation kinetics and microstructure of carbide and diboride based ceramics. Dissertation. Technische Universität Clausthal, 2005.

[34] Telle R. The quasi ternary system TiB_2–CrB_2–WB_2 between 1500 and 1900 ℃ and the related quasi binary subsystems. *J Eur Ceram Soc* 2019, **39**: 3677–3683.

[35] Telle R. A new ternary phase in the system TiB_2–CrB_2–WB_2. *Solid State Sci* 2020, **101**: 106120.

[36] Wang YJ, Yan QZ. Microstructure and strengthening mechanism of grain boundary strengthened W–ZrB_2 alloy. *J Mater Res Technol* 2020, **9**: 4007–4015.

[37] Silvestroni L, Failla S, Gilli N, *et al*. Disclosing small scale length properties in core–shell structured B_4C–TiB_2 composites. *Mater Des* 2021, **197**: 109204.

[38] Roa JJ, Jimenez-Pique E, Verge C, *et al*. Intrinsic hardness of constitutive phases in WC–Co composites: Nanoindentation testing, statistical analysis, WC crystal orientation effects and flow stress for the constrained metallic binder. *J Eur Ceram Soc* 2015, **35**: 3419–3425.

[39] Roa JJ, Sudharshan Phani P, Oliver WC, *et al*. Mapping of mechanical properties at microstructural length scale in WC–Co cemented carbides: Assessment of hardness and elastic modulus by means of high speed massive nanoindentation and statistical analysis. *Int J Refract Met Hard Mater* 2018, **75**: 211–217.